Materials Advances

ROYAL SOCIETY OF CHEMISTRY

PAPER

View Article Online
View Journal | View Issue

Cite this: *Mater. Adv.*, 2025, 6, 4725

Functionalized MIL-125(Ti)-based high-performance triboelectric nanogenerators for hygiene monitoring†

Anjaly Babu,[a] Navaneeth Madathil,[a] Rakesh Kumar Rajaboina,[a] Hitesh Borkar,[a] Kamakshaiah Charyulu Devarayapalli,[b] Yogendra Kumar Mishra,[c] Sugato Hajra,[d] Hoe Joon Kim,[d] Uday Kumar Khanapuram *[a] and Dae Sung Lee *[b]

Received 28th March 2025,
Accepted 18th May 2025

DOI: 10.1039/d5ma00283d

rsc.li/materials-advances

Metal–organic frameworks (MOFs) have emerged as promising materials for energy harvesting through triboelectric nanogenerators (TENGs). Strategic incorporation of functional groups within the MOFs offers a method for tailoring the surface and functional properties of composite materials, thus leading to enhancement in the performance of TENGs. This study investigates the relationship between functional groups and TENG performance using MIL-125(Ti), specifically incorporating electron-donating (NH_2) and electron-withdrawing (NO_2) groups. MIL-125(Ti)-NH_2@silicone composite film, along with aluminum, produces a maximum voltage and current of 512 V and 130 μA, and a power density of 6.75 W m^{-2}, which is twice the power density of the pure silicone-based TENG. The enhancement of TENG output is attributed to the functionalization of MIL-125, which results in the change of dielectric constant, work function and tuning of the band gap of the composite materials. Furthermore, a novel TENG-based door sensor was demonstrated for the application of a smart alert hygiene system. This sensor efficiently tracks the number of washroom usages by detecting door movements. The real-time data generated by the system notifies the cleaning staff, ensuring the maintenance of a cleaner and more hygienic washroom environment. The study highlights the potential of functionalized MIL-125(Ti)-based TENGs for efficient energy harvesting and sustainable hygiene monitoring.

1. Introduction

In recent years, triboelectric nanogenerators (TENGs) have emerged as a promising clean and sustainable energy source in the field of the internet of things (IoT), self-powered portable and implantable electronic devices.[1–6] The working principle of TENGs relies on the combined effect of contact electrification and electrostatic induction for converting mechanical energy to electrical energy.[7–10] However, the relatively low output power density of TENGs presents a trade-off for real-life applications. Apart from choosing suitable triboelectric pairs, various strategies have been employed, such as surface patterning, surface functionalization, doping, and the use of high dielectric materials as fillers which can significantly improve the charge-inducing or charge-trapping capabilities of the triboelectric materials, ultimately leading to improved performance of TENG devices.[11–16]

In the majority of TENG devices, polymer materials are chosen as dominant triboelectric materials considering their several properties, such as flexibility, lightweight, biocompatibility, ease of fabrication, and cost-effectiveness.[17–19] Currently, utilizing MOF materials as functional fillers for polymer materials has gained prominence in the field of TENGs.[20–25] MOFs are highly crystalline three-dimensional materials with networks of metal ions and organic ligands having unique properties such as tunable pore size, high surface area, and excellent chemical and thermal stability.[26] Strategic embedding of these MOFs allows for significant alteration of surface and dielectric properties of the polymer, thereby enhancing the TENG output performances. This optimization unlocks the potential of TENGs towards advanced

[a] Department of Physics, Energy Materials and Devices (EMD) Lab, National Institute of Technology, Warangal, 506004, India. E-mail: kanapuram.udaykumar@nitw.ac.in
[b] Department of Environmental Engineering, Kyungpook National University, Buk-gu, Daegu, 41566, Republic of Korea. E-mail: daesung@knu.ac.kr
[c] Smart Materials, NanoSYD, Mads Clausen Institute, University of Southern Denmark, Alsion 2, 6400, Sønderborg, Denmark
[d] Department of Robotics and Mechatronics Engineering, Daegu Gyeongbuk Institute of Science and Technology, Daegu, 42988, South Korea

† Electronic supplementary information (ESI) available. See DOI: https://doi.org/10.1039/d5ma00283d

sensors and wearable electronics.[27–30] The focus of traditional TENG development relies heavily on discovering new MOFs with desirable structures. However, recent advancements have opened a new avenue with functionalized MOFs, demonstrating their effectiveness and offering a promising alternative strategy for boosting TENG output.

Guo *et al.* demonstrated improved TENG performance by integrating fluorinated MOFs as a bifunctional filler to polymer PDMS.[31] The F-atom in the MOF boosts the charge-inducing and charge-trapping capabilities as well as the hydrophobicity of the composite film. Coupled with aluminum, the F-MOF-PDMS composite film shows an exceptional leap in power density of around 52 μW cm^{-2}, which is 11 times that of the pristine PDMS. Yong-Mei Wang *et al.* showed a remarkable improvement in performance by introducing UiO-66-NH_2 with a micro dimension diameter of around 400 nm into PDMS.[32] This chemically modified UiO-66-NH_2 contributes to the surface roughness of the composite film, resulting in more effective charge transfer. The electron-withdrawing amine group of organic ligand terephthalic acid in UiO-66-NH_2 greatly influences the surface potential of the composite film, forming a fundamental factor in improving the TENG output performances. The UiO-66-NH_2 composite-based TENG produces an open circuit voltage (V_{oc}) of 4 times the pure PDMS-based TENG. Y. Wang *et al.* extended their work by replacing the amine group in UiO-66-NH_2 with highly electronegative F-atoms as UiO-66-4-F.[32] The incorporation of UiO-66-4-F, containing tetrafluoro terephthalic acid as organic ligands with four F-atoms each, demonstrably improves the performance of the composite film in TENGs. This enhancement can be attributed to the strong electron-withdrawing ability of the F-atoms, which elevates the charge-inducing and charging-trapping site of the composite film. The UiO-66-4F@PDMS-based TENG produced an output voltage and power density of 937.8 V and 38.7 W m^{-2}, which is the highest among the reported MOF-based TENG devices.[33] Hence, the above studies highlight that strategically incorporating specific functional groups into the MOF allows the properties of the composite materials to be precisely tailored, thus leading to substantial improvement in TENG performance.

Titanium-based MOFs, particularly MIL-125(Ti), have emerged as a prominent material for diverse applications, which stems from the unique properties of its Ti^{4+} metal ion, which exhibits favorable redox activity, and strong metal–ligand interactions to the rigid and robust framework. In MIL-125(Ti), Ti^{4+} metal ions and terephthalic acid form the basic building block of the framework.[34] However, besides possessing biocompatibility, exceptional stability, low cost, and non-toxic, its application in the TENG field remains relatively unexplored. Recently, for the first time, Kakim *et al.* reported a MIL-125(Ti)-based TENG, where MIL-125(Ti) was integrated into the silicone (Ecoflex) polymer and was used as a composite film.[2] The study reveals that MIL-125(Ti) improves the charge-trapping and charge-inducing properties of the composite film. MIL-125(Ti)/Ecoflex produced an V_{oc} and short circuit current (I_{sc}) of around 305 V and 13 μA. The developed flexible TENG generated a power density of 1.5 W m^{-2}, which is two-fold the response of a pristine Ecoflex-based device. The fabricated device is a self-powered sensor embedded into a robotic gripper trained *via* machine learning to identify the various grasping objects.[35] The detailed literature on MIL-based triboelectric nanogenerators is presented in Table 1. The present work focuses on functionalized MIL-125(Ti) materials with electron-donating (NH_2) and electron-withdrawing (NO_2) groups to study the underlying relationship between functional groups and TENG output performance. While the effects of work function on TENG output have been widely explored, the concept of bandgap tuning through functional groups remains relatively underexplored. Interestingly, bandgap tuning offers similar advantages as work function modification, enabling effective control over charge transfer and trapping in the triboelectric layers.[36] By employing bandgap tuning through functional groups, we delve into the unexplored potential of bandgap modulation, which, like work function alterations, significantly affects TENG output. Our study suggests that the output performance of the TENG device follows the trend silicone < MIL-125(Ti)@silicone < MIL-125(Ti)-NO_2@silicone < MIL-125(Ti)-NH_2@silicone, a progression that is well-correlated with changes in work function, and dielectric constant. The MIL-125(Ti)-NH_2@silicone produced maximum V_{oc} and I_{sc} of 512 V and 130 μA, respectively. At an external load resistance of 10 MΩ, the MIL-125(Ti)-NH_2@silicone-based TENG device attained a peak power density of 6.75 W m^{-2}, twice the power density of the pure silicone-based TENG. The

Table 1 The detailed literature on MIL-based triboelectric nanogenerators

S. no.	Electrode-1	Electrode-2	Voltage (V), current (μA)	Power density	Applications	Ref.
1	MIL-88A	FEP/Kapton/EC	90, 2.5	16.2 mW m^{-2}	Powering electronic devices	37
2	NH_2-MIL-101(Fe,Cu) particles with CNF	FEP	194, 14	20.3 μW cm^{-2}	Powering LEDs	38
3	MIL-88A-$BaTiO_3$-PDMS	Kapton	486, 160	5.82 W m^{-2}	Sound energy harvesting	23
4	MIL-100 (Fe)	FEP	75, 5	15 mW m^{-2}	Waste water treatment	39
5	MIL-101(Cr)-PY	PTFE	825, 11	25.03 W m^{-2}	Degradation of organic pollutants	40
6	MIL-101 (Cr)@PVDF	Al	414, 14.6	568.8 μW cm^{-2}	Self-powered triggering sensor	41
7	MIL-100-PAN	ZIF-8-PAN	100, 1.3	18.37 mW m^{-2}	Self-powered humidity sensor	42
8	MIL-125@Ecoflex	Carbon fibre cloth	305, 14.9	1.5 W m^{-2}	Robotic grippers	2
9	MIL-125-NH_2@silicone	Al	512, 130	6.7 W m^{-2}	Door sensor hygiene monitoring system	This work

fabricated device was used to light up 460 LEDs and run low-power electronic devices. Finally, a novel TENG-based door sensor is introduced by utilizing MIL-125(Ti)-NH_2@silicone and aluminum as a triboelectric layer, which tracks washroom usage sustainably based on the movement of the door. This real-time data alerts the cleaning staff, thus promoting a clean and healthy washroom.

2. Experimental methods

2.1 Materials

Tetra butyl titanate (TNBT), terephthalic acid (H_2BDC), 2-aminoterephthalate (NH_2-H_2BDC), 2-nitroterephthalate (NO_2-H_2BDC), dimethyl formamide (DMF), and methanol (MeOH) were purchased from Sigma Aldrich and used without any further purification. Liquid silicone rubber and catalyst were procured from Chemzest Techno products Pvt Ltd.

2.2 Synthesis of MIL-125(Ti) and MIL-125(Ti)-X (X = NH_2, NO_2)

All the samples were prepared based on the previously reported procedure with slight modifications.[43–45] The synthesis procedure of MIL-125(Ti) followed is briefly: 1 g of H_2BDC was added to a 20 ml solution containing methanol (MeOH) and DMF taken in a 1 : 9 ratio and sonicated at room temperature for 10 min. Subsequently, 0.52 ml of TNBT was added dropwise under magnetic stirring for 30 min. The resultant transparent solution was then transferred to a 100 ml Teflon-lined autoclave and was isothermally maintained at 150 °C for 24 h. After cooling down naturally, the white precipitate was collected by filtration and washed thoroughly with DMF and MeOH several times, followed by drying at 80 °C overnight and labelled as MIL-125(Ti). A schematic diagram of the synthesis procedure of MIL-125(Ti) and a photograph of the obtained powder is shown in Fig. 1a. Similarly, MIL-125(Ti)-NH_2 was prepared following the above procedure by replacing H_2BDC with NH_2-H_2BDC and keeping the reaction for 72 h.

MIL-125(Ti)-NO_2 was prepared by dissolving 338 mg NO_2-H_2BDC into a solution containing methanol and DMF taken in a 1 : 9 ratio. Under continuous stirring, 105.2 mg of the as-prepared MIL-125(Ti) was added and further transferred to a Teflon-lined autoclave and maintained at 150 °C for 24 h. A further similar procedure of MIL-125(Ti) was followed to obtain MIL-125(Ti)-NO_2.

2.3 Preparation of MIL-125(Ti)-X@silicone films

For the preparation of pure silicone rubber film, the catalyst and elastomers were mixed in 1 : 10 ratios and manually stirred for 20 min. Subsequently, the mixture was transferred to a Petri dish, which was then dried at room temperature overnight. For the preparation of MIL-125(Ti)-X@silicone film (X = NH_2, NO_2), a predetermined amount of the as-prepared MIL-125(Ti) and MIL-125(Ti)-X (X = NH_2, NO_2) was added to elastomers and manually stirred. Furthermore, the catalyst part was added, and the mixture was once again agitated by pouring the mixture into a Petri dish and dying at room temperature. Fig. 1b shows a schematic illustration of the MIL-125@silicone film. From Fig. 1c it can be seen that all the self-standing films are flexible in nature.

2.4 Fabrication of the device

Initially, a square-shaped cardboard sheet was cut down into the required dimensions of 8 cm × 8 cm. Then, an aluminum electrode, along with the prepared flexible composite films, was attached to one of the cardboard sheets. Subsequently, to the other cardboard sheet, another aluminum electrode, which also serves as an opposite frictional layer has been attached. Both these cardboard sheets are stacked over each other, with the triboelectric layers facing opposite. To provide a spacing between these triboelectric layers for effective contact and separation, four elastic sponges are placed at the corners of

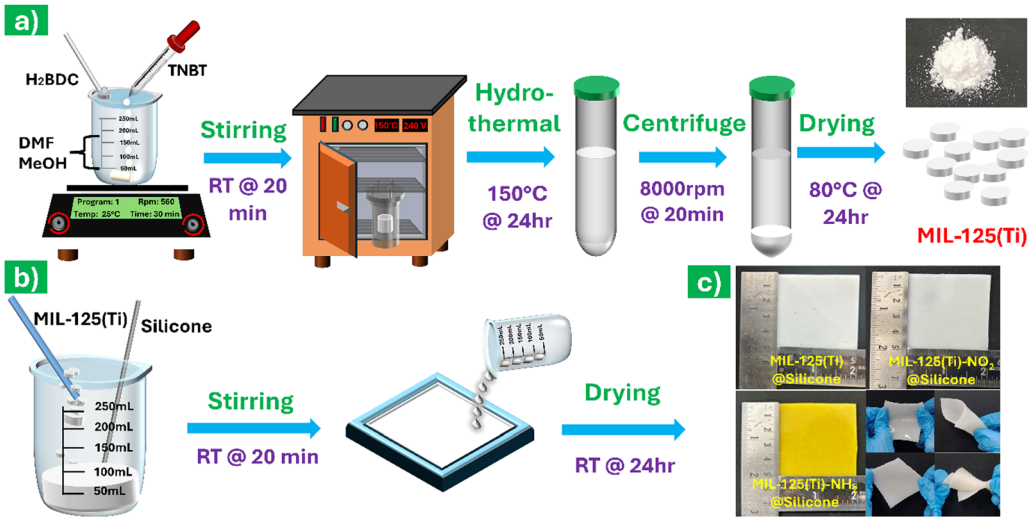

Fig. 1 Schematic illustration of the synthesis of (a) MIL-125(Ti) and (b) MIL-125(Ti)@silicone film, and (c) photographs of the obtained composite films.

these cardboard sheets. The detailed fabrication steps are given in Fig. S1 (ESI†).

2.5 Characterization

The structural and morphological studies were carried out by X-ray diffraction (XRD, Xpert powder) & field emission scanning electron microscopy (FESEM) equipped with an energy-dispersive X-ray spectroscopy (EDS) detector (JEOL JSM IT-800). The functional groups in the sample were examined using a Fourier-transform infrared spectrometer (FT-IR, Shimadzu 8201 PC Fourier Transform Infrared). For optical studies, diffuse reflectance UV-vis spectra of the samples were recorded on a UV-vis spectrophotometer (Agilent Technology, Cary 5000). Ultra-violet spectroscopy (UPS) measurements were performed with a ThermoFisher (NEXSA), microfocus monochromatic X-ray source: Al-Kα (1486.6 eV).

3. Results and discussion

Fig. 2a shows the XRD pattern of MIL-125(Ti) and its derivative powder form prepared by the hydrothermal method and simulated XRD pattern (cif-file COD 7211159).[46] The XRD patterns

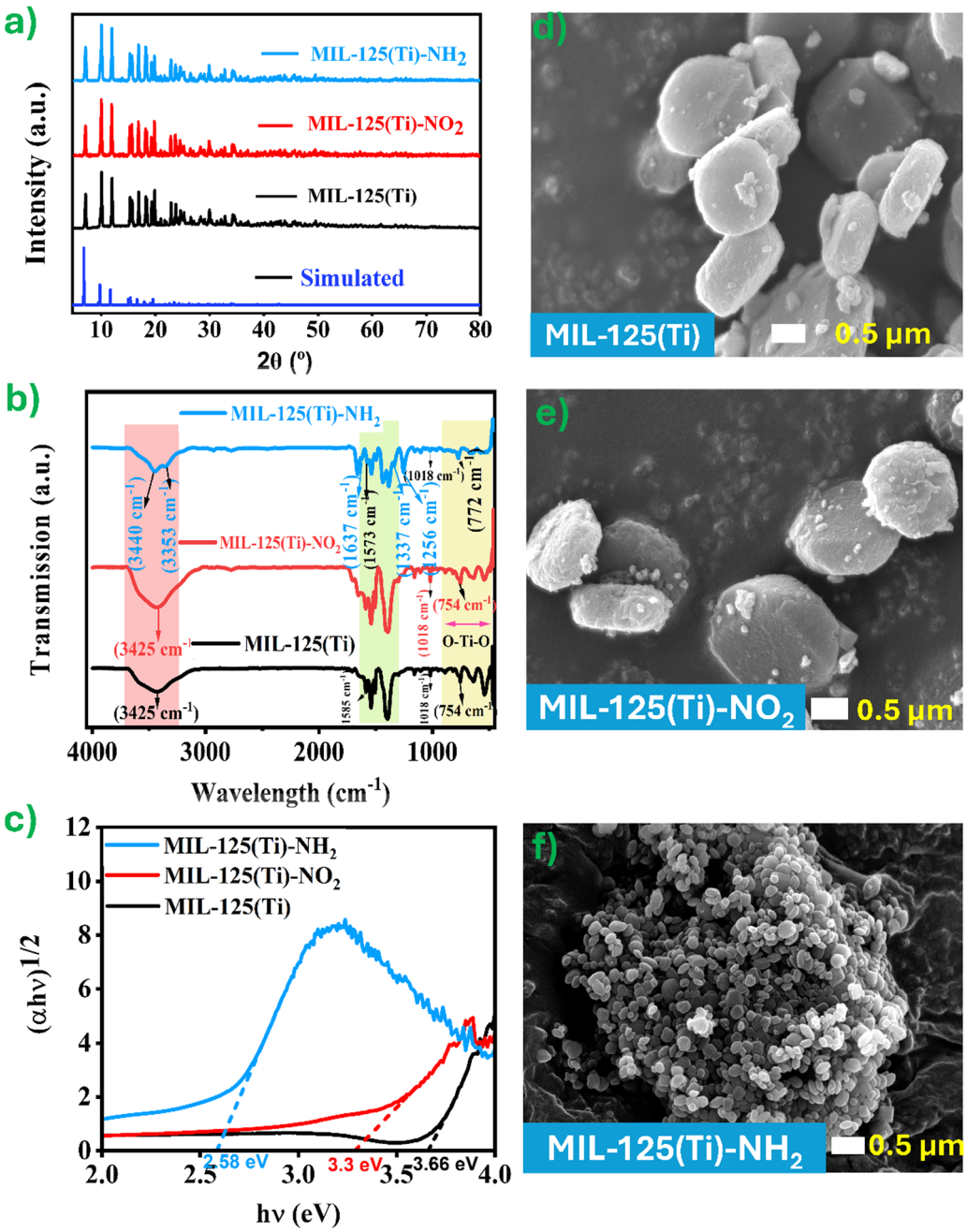

Fig. 2 (a) XRD pattern, (b) FTIR spectra of the prepared MIL-125(Ti) derivatives, (c) band gap energy estimated from diffuse reflectance UV-vis spectra, (d)–(f) FESEM images of MIL-125, MIL-125(Ti)-NO_2, and MIL-125(Ti)-NH_2, respectively.

show high crystallinity of both the ligand and metal clusters.[47] The crystal structure of MIL-125(Ti) remains unchanged following the functionalization with amine and nitrile (nitro) groups, indicating that substituting a hydrogen atom with an $-NH_2$ or NO_2 group does not affect the framework structure.[48–51] The prominent diffraction peaks centred at 7.0°, 9.94°, 11.9°, 16.8°, 18.19°, 19.26°, 22.82°, and 23.72° correspond to the lattice planes of MIL-125 and MIL-125-X, and are in agreement with the previously reported works.[49,52–55]

The chemical bond and functional groups present in the prepared MIL-125(Ti) and its functional derivative samples were studied by using FT-IR spectroscopy within the range of 4000 cm^{-1} to 500 cm^{-1} and are depicted in Fig. 2b. The broad absorption band in the range of 3425 cm^{-1} indicates the O–H stretching of H_2O, suggesting water absorption of the surface. In the case of MIL-125(Ti)-NH_2, peaks at 3446 cm^{-1} and 3357 cm^{-1} correspond to the symmetric and asymmetric vibrations of the amine group, confirming the presence of independent amine groups present without binding partners.[51,56,57] The broad band observed around 3430 cm^{-1} for the MIL-125(Ti)-NH_2 sample can be attributed to solvent molecules trapped within the pores. This includes the stretching vibrations of O–H groups from the adsorbed water, which emerge in this wavelength range.[51] The vibration modes of the linker carboxylate groups correspond to the peak observed in the region of 1397 cm^{-1} to 1709 cm^{-1}, whereas the vibration of O–Ti–O corresponds to the band found in the region of 500 cm^{-1} to 800 cm^{-1}. Apart from a few additional peaks observed at 1637 cm^{-1}, which are assigned to the N–H bond, and the peaks at 1384 cm^{-1} and 1256 cm^{-1} corresponding to stretching vibrations of C–N bonds, MIL-125(Ti)-NH_2 possess a similar spectrum of MIL-125(Ti). The asymmetric peak of the metal oxo cluster and organic ligand coordination characteristic peak (O–C–O) are observed for both MIL-125(Ti) and MIL-125(Ti)-NO_2 at 1585 cm^{-1}, this characteristic peak exhibited a red shift in the case of MIL-125(Ti)-NH_2 at 1573 cm^{-1}. The $-NH_2$ group in NH_2BDC causes this redshift, as its electron-donating property leads to a resonance effect, consequently lowering the frequency of the O–C–O signal.[58] Amine group presence can be observed by the additional peak due to the characteristic absorption of the C–N stretching vibration between the carbon atom bonded with the benzene ring and the nitrogen atom bonded with the amine group at 1337 cm^{-1}.[59] The peak observed at 1532 cm^{-1} is associated with the stretching vibrations of the NO_2 group in the MIL-125(Ti)-NO_2.[60]

To investigate the optical properties of MIL-125(Ti) and its functional derivatives, UV-vis diffuse reflectance spectra measurements were carried out. For MIL-125(Ti) and MIL-125(Ti)-NO_2, the absorption bands are below 350 nm, as shown in Fig. S2 (ESI†). Whereas the absorption band of MIL-125(Ti)-NH_2 clearly shows a red shift towards the visible range, with the band edge extending 550 nm. The redshift of the absorption band edge might be caused by the ligand to meta charge transfer (O–Ti) in the inorganic clusters[48]. The charge transfer process in the inorganic clusters is influenced by amine group ligands, and the same observations are reported in the literature.[48,61]

The engineering of the Ti-based MOF bandgap has been reported by several researchers. The introduction of functional groups to the terephthalic organic ligand is shown to drastically impact the electronic structures of the parental MIL-125(Ti), ultimately leading to a reduction in the band gap. Fig. 2c reveals that the optical band gap of the MIL-125(Ti) and its derivatives, calculated to be 3.6 eV, 3.3 eV, and 2.58 eV for MIL-125(Ti), MIL-125(Ti)-NO_2, and MIL-125(Ti)-NH_2, respectively.[43,62]

The FESEM images of MIL-125(Ti), MIL-125(Ti)-NO_2, and MIL-125(Ti)-NH_2 are shown in Fig. 2(d–f). The FESEM signifies the surface morphology of the as-prepared MIL-125(Ti) and MIL-125(Ti)-NO_2 exhibits a tablet-like structure with an average particle size of ~1–2 μm (Fig. 2d and e). Notably, while MIL-125(Ti)-NH_2 displays a comparable morphology, a reduction in particle size of 200 to 500 nm is observed (Fig. 2f). This could be attributed to the introduction of an amine group, which can alter the coordination environment, resulting in faster nucleation and thus reducing the particle size. The similar behaviour of particle size reduction has been reported in the literature for the MIL-125-NH_2.[63–65] The EDX spectrum also confirms the existence of Ti, C, and O, which are the primary constituent elements of MIL-125(Ti), and its derivatives are presented in Fig. S3 (ESI†).

Fig. 3a represents the XRD spectrum of the MOF-silicone composite films. The XRD spectrum of the composite film has the characteristics peaks of MIL-125(Ti)-X and a broad diffraction peak from the silicone polymer, indicating that the crystallinity of MIL-125(Ti)-X in the nanocomposite film was maintained as well. The characteristics peak at 12.5° and 22.4° correspond to the pure silicone, whereas the peaks at 7.05°, 9.65°, 15°, and 19.4° correspond to MIL-125(Ti)-X in the composite film, indicating that MIL-125(Ti)-X is mixed well in the silicone polymer.

The FTIR spectrum of silicone aligns well with previously reported works.[66] As shown in Fig. 3b, the characteristic band at 2962.8 cm^{-1} corresponds to the stretching vibrations of C–H bonds in the methyl groups. The peak at 1408 cm^{-1} is associated with the asymmetric stretching vibrations of the Si–CH_3 bond, while the bands at 1259 cm^{-1} and 793 cm^{-1} correspond to the Si–C stretching vibrations of Si–CH_3 and Si–$(CH_3)_2$, respectively. Additionally, the FTIR spectra of the MIL-125(Ti)-X@silicone film showed no band shift or new band formation, suggesting that there was no chemical interaction between the silicone and MIL-125-X.

From Fig. 3c, the calculated optical band gap of silicone is ~5.1 eV. However, the addition of MIL-125-X tends to reduce the band gap to 2.4 eV, 1.8 eV, and 1.34 eV for MIL-125(Ti)@silicone, MIL-125(Ti)-NO_2@silicone, and MIL-125(Ti)-NH_2@silicone, respectively. Fig. 3(d–f) presents FESEM images of the composite film, showing the random distribution of MIL-125-X nanoparticles embedded within the silicone matrix, which leads to an increased surface roughness of the composite. Additionally, FESEM images of the MIL-125(Ti)-X@silicone composite films for all concentrations are provided in Fig. S4 (ESI†).

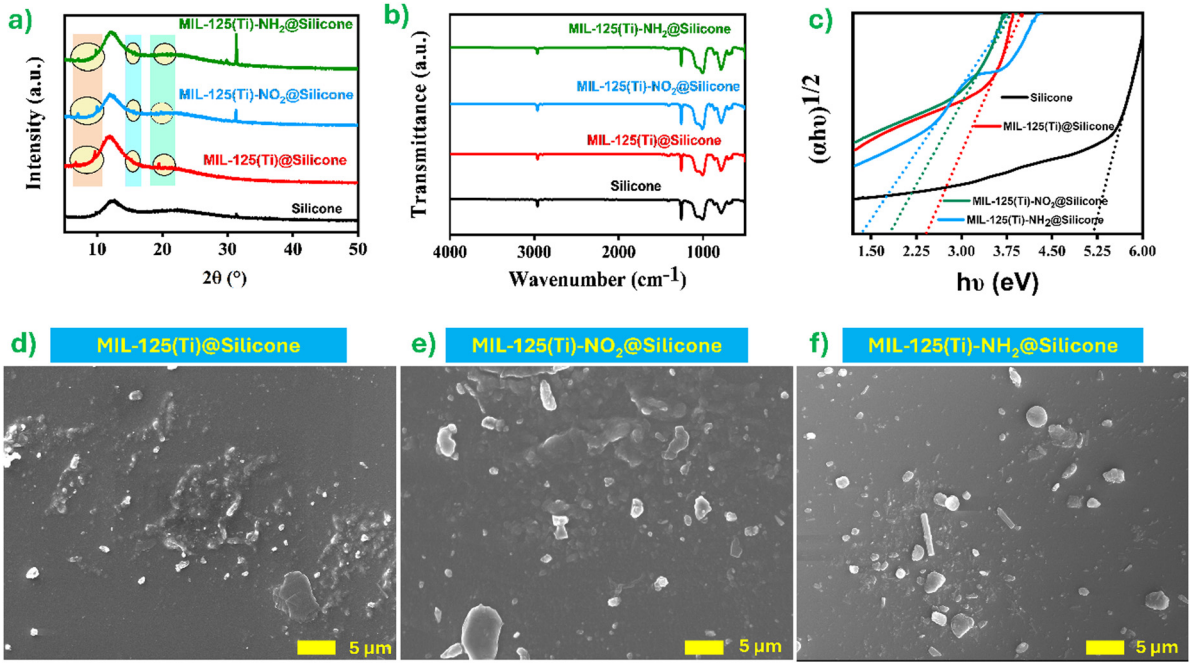

Fig. 3 (a) XRD pattern, (b) FTIR spectra, (c) band gap energy estimated from diffuse reflectance UV-vis spectra of the prepared MIL-125(Ti)-X@silicone films and (d)–(f) FESEM images of the prepared MIL-125(Ti)-X@silicone films.

To investigate the output performance of the TENG devices, a group of tests were performed to measure the V_{oc} and I_{sc} under stable hand tapping force (~10 N) and frequency (~4 Hz). Fig. 4a shows the V_{oc} and I_{sc} response of the TENG device with six distinct polymer sheets while MIL-125(Ti)-NH_2@silicone is the fixed opposite triboelectric layer of the devices. The maximum triboelectric response of V_{oc} ~ 512 μA and I_{sc} ~ 130 μA was achieved when the aluminum served as the opposite frictional layer to MIL-125(Ti)-NH_2@silicone.

This test provides a testimony that the MIL-125(Ti)-NH_2@silicone will be acting like a negative triboelectric material showing lower output with other negative materials like FEP, Teflon, silicone, and PET, but significantly higher output when paired with positive materials like Kapton, PMMA, and aluminum, aligning with the triboelectric series. These results are in agreement with previously reported literature and consistent with the triboelectric series.[67] This can be understood, as in the case of FEP, Teflon, silicone, and PET, all are negative materials, and the smaller difference in the affinity with MIL-125(Ti)-NH_2@silicone could be the reason for the lower device output performance. Meanwhile, Kapton, PMMA, and aluminum are positive materials, and the difference in affinity would be higher as a result of higher output performance. Moreover, aluminum is more positive in nature than Kapton and PMMA. Therefore, the output performance has been seen to be higher for the aluminum and MIL-125(Ti)-NH_2@silicone than for any other pairs. Furthermore, pristine silicone with an aluminum pair has produced an output voltage of 300 V and 60 μA (see Fig. S5, ESI†). The above result confirms the improvement in the output performance of the TENG with the addition of MOFs.

To investigate the impact of MOF concentration in the silicone matrix, the weight percentage of MIL-125(Ti) was varied from 0.5% to 2.5% (w/w ratio) to assess its effect on TENG output performance. Additionally, to examine the influence of functionalization, MIL-125(Ti) films were used along with functionalized variants incorporating an electron-withdrawing group (MIL-125(Ti)-NO_2) and an electron-donating group (MIL-125(Ti)-NH_2). For all these materials, the doping concentrations were similarly varied from 0.5% to 2.5% within the silicone matrix. This result reveals a considerable change in the output performance of the TENG with the introduction of functional groups. The performances of unfunctionalized MIL-125@silicone yielded V_{oc} and I_{sc} of 352 V and 64 μA. When functionalized with an electron-withdrawing nitro group NO_2, electron-donating amine group NH_2 leads to an enhanced output performance of the TENG. When MIL-125(Ti) is functionalized with the NO_2 group, the MIL-125(Ti)-NO_2@silicone TENG exhibited V_{oc} and I_{sc} of ~468 V and 108 μA, respectively. Notably, the maximum recorded V_{oc} and I_{sc} of ~512 V, and 130 μA were attained by the MIL-125(Ti)-NH_2@silicone TENG device (Fig. 4(b and c)). The amine modification of MIL-125(Ti) yielded a remarkable two-fold increase in I_{sc} relative to the unfunctionalized MIL-125(Ti)@silicone TENG device. Hence, the observed data for the output performance of the TENG device follows the trend silicone < MIL-125(Ti)@silicone < MIL-125(Ti)-NO_2@silicone < MIL-125(Ti)-NH_2@silicone.

Furthermore, to elucidate the influence of functional groups, work function and its subsequent effect on TENG performance were evaluated through ultraviolet-photo spectroscopy (UPS) measurements. The measured work functions for

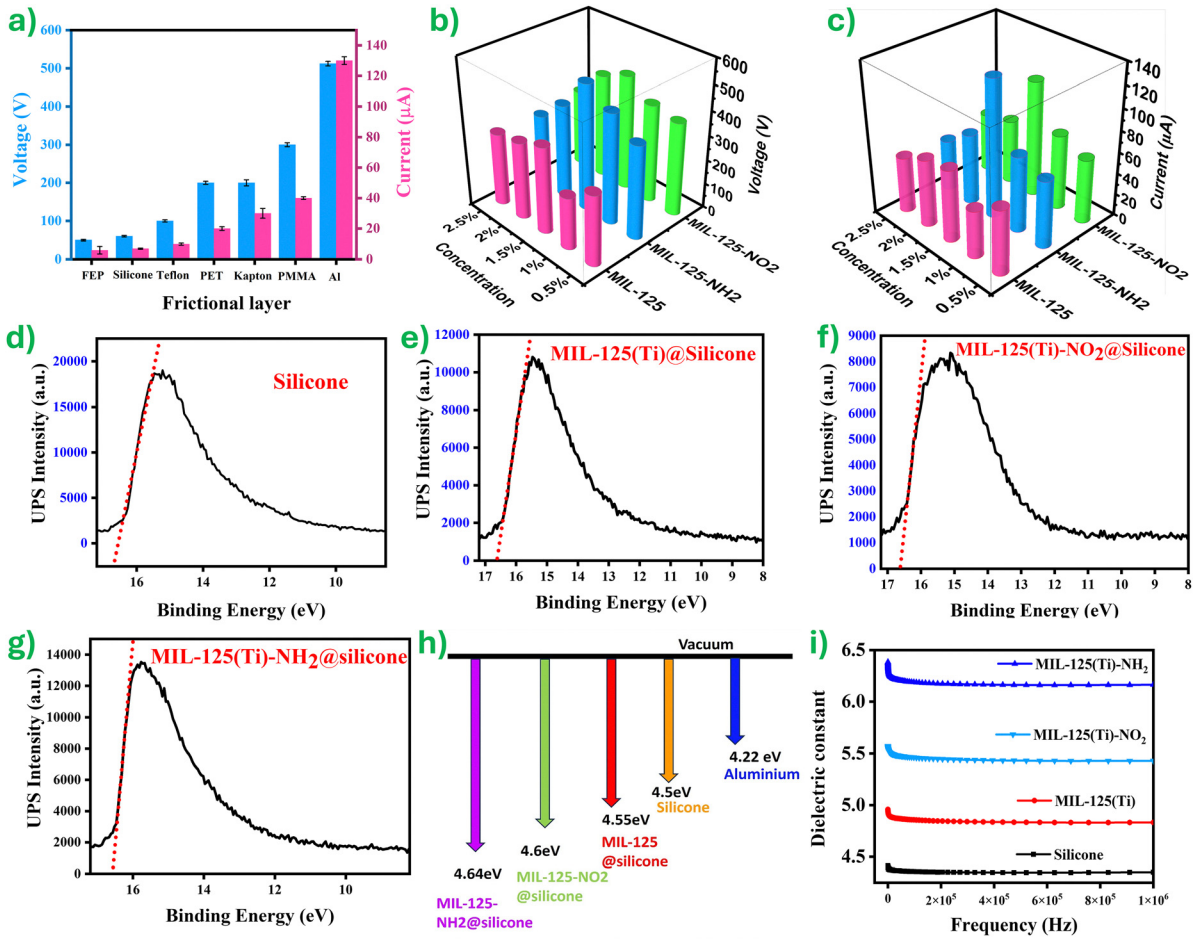

Fig. 4 (a) The output response of MIL-125(Ti)-NH_2@silicone TENG with respect to different frictional materials. (b) and (c) V_{oc} & I_{sc} of MIL-125(Ti)@silicone, MIL-125(Ti)-NH_2@silicone, and MIL-125(Ti)-NO_2@silicone. (d) UPS measurement of pure silicone, (e) MIL-125(Ti)@silicone, (f) MIL-125(Ti)-NO_2@silicone, and (g) MIL-125(Ti)-NH_2@silicone. (h) Work function value comparison for the silicone film, MIL-based composite films, and aluminum. (i) Dielectric constant of the obtained films.

the MIL-125(Ti)-X@silicone composites are presented in Fig. 4(d–g). The results show an increasing trend in work function with the introduction of functional groups: MIL-125(Ti)@silicone, MIL-125(Ti)-NO_2@silicone and MIL-125(Ti)-NH_2@silicone exhibit 4.55 eV, 4.6 eV and 4.64 eV, respectively. This can be attributed to the electron-donating nature of the amine groups, which slightly increases the material's work function by influencing the electron density near the surface. Notably, the amine functionalization in MIL-125(Ti)-NH_2@silicone resulted in the largest work function difference compared to aluminum (4.22 eV) (Fig. 4h). This significant disparity aligns perfectly with the principle in TENGs where a larger work function difference between contacting surfaces facilitates a greater transfer of electrons, ultimately leading to a higher electrical output performance of the TENG.

To study the dielectric influence on the output response of the TENG, the permittivity of the films prepared was measured across the frequency range from 10^2 to 10^6 Hz at room temperature and is depicted in Fig. 4i. The dielectric constant of amine-functionalized MIL-125 exhibits a remarkable increase reaching a value of 6.1, which is 1.8 times greater than the value of 4.3 measured for pure silicone at the same frequency of 6×10^5 Hz. This significant enhancement likely stems from the presence of the polar amine group, which interacts with the opposite charge within the polymeric chain, generating additional dipoles.[68,69] These dipoles increase the capacitances of the composite film, thereby offering more charge trapping sites and thus improving the triboelectric charge density and hence the TENG output.[31] A similar trend was reported by filler-incorporated composite-based nanogenerators in the literature.[67,70,71]

In the current study, the functionalized MIL-125(Ti) materials exhibited enhanced surface roughness (see Fig. S6, ESI†). The functionalized MIL-125(Ti)-NH_2 materials exhibited enhanced surface roughness, which significantly contributed to the improved performance of the TENG devices. The rough surface increased the area available for contact, thereby enhancing the charge generation potential. Among the composites, the MIL-125(Ti)-NH_2@silicone composite with the highest surface roughness demonstrated superior output performance,

including the highest V_{oc}, I_{sc}, and power density. This highlights the critical role of surface roughness in optimizing the charge generation capability of the TENG devices.

From Fig. 4(b and c), it is clear that the 1.5 weight percentage concentration of MOF is showing higher electrical output among all the devices. The trend in the TENG with different MOF concentrations is similar to the reported trends in the literature.[42,67,72,73] The increasing TENG output with the increase of MOF concentration in the silicone matrix can be attributed to changes in the dielectric constant, which is well reported in the literature.[73–75] The further increase of MOF concentration (greater than 1.5 weight percent) in the silicone matrix resulted in decreased output. This could be due to the agglomeration of MOF particles in the silicone polymer, which could lead to void formation between the polymer and MOF particles after 1.5% w/w.[76] Therefore, from the above results, the TENG device with 1.5% w/w was considered the optimal concentration of MIL-125(Ti)-NH_2 in the silicone polymer matrix. The detailed electrical characteristics of the MIL-125(Ti)-NH_2-based TENG are presented in the next section.

Fig. 5(a and b) present the switching polarity test results for the MIL-125(Ti)-NH_2@silicone TENG device, confirming that the observed electrical signal originates from the TENG device itself and not from any noise or artifacts. This conclusion is supported by the polarity reversal of the output signal, whereas noise remains unchanged. The working mechanism of MIL-125(Ti)-NH_2@silicone TENG under one cycle of operation is shown in Fig. 5c. In the original state, the device is in a neutral state; hence, the net output of the device is zero Fig. 5c(i). When the TENG device is pressed, both the frictional layers come in full contact with each other; as per the work function difference, an equal number of positive and negative charges accumulate on the aluminum and MIL-125(Ti)-NH_2@silicone film, respectively, as depicted in Fig. 5c(ii). When the triboelectric

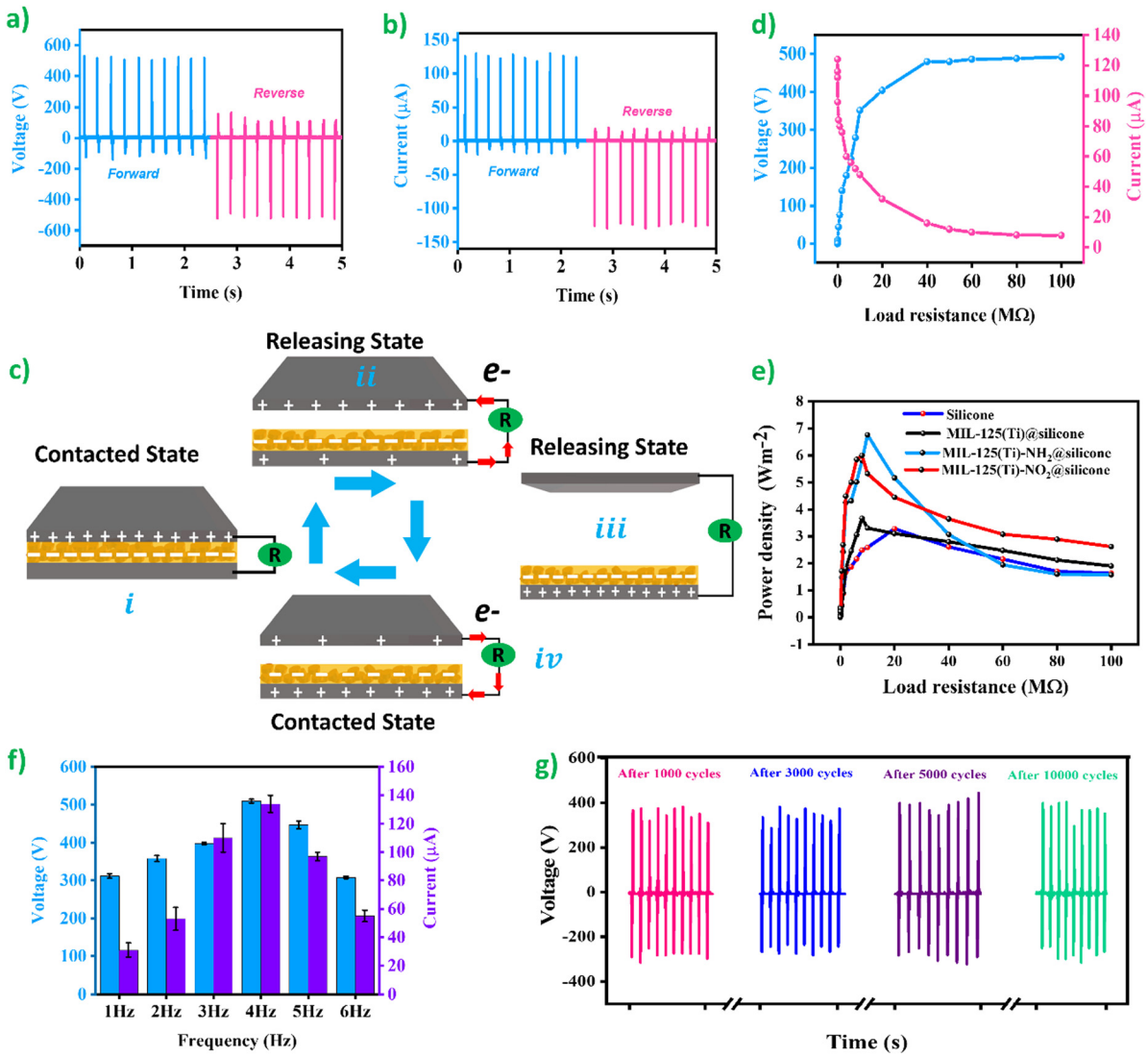

Fig. 5 (a) and (b) V_{oc} & I_{sc} of the MIL-125(Ti)-NH_2@silicone TENG, and (c) working mechanism of the TENG device. (d) Voltage and current response as a function of various load resistances. (e) Power density of the TENG devices. (f) Voltage and current response with a variation of hand tapping frequency. (g) Stability of the response of MIL-125(Ti)-NH_2@silicone TENG devices over 10 000 cycles.

layers begin to part away, a potential difference is induced across the electrode, leading to the flow of electrons from the bottom aluminum electrode to the top electrode until it reaches an equilibrium state, as shown in Fig. 5c(iii and iv). Under an equilibrium state of the device, the introduction of external force will cause the electron to flow in the reverse direction from the top to bottom aluminum electrode due to a decrease in the potential difference across the electrodes, as shown in Fig. 5c(v). This periodic change in the potential difference across the device produces an alternating current in the external circuit.

Furthermore, the variations in the TENG output voltage and current within the range of 1 kΩ to 100 MΩ load resistances were measured and presented in Fig. 5d. The result revealed that as the external resistance increased, the output voltage exhibited a rise, while the current demonstrated a contrary trend. Additionally, the power density of the TENG device was calculated by using the formula $P = (V \times I)/A$, where V and I represent the voltage and current at the corresponding resistance, and A denotes the active contact area of the triboelectric layer.[77] The power density trend of all the TENG devices is depicted in Fig. 5e. The highest power density was observed for the MIL-125(Ti)-NH_2@silicone device. In the case of MIL-125(Ti)-NH_2@silicone, the instantaneous power density exhibited an initial increase followed by a decrease. At an external resistance of 10 MΩ, the peak output power density reached 6.75 W m^{-2}, exceeding twice the maximum power density of the pure silicone-based TENG, which is estimated to be 3.2 W m^{-2}. The power density of the NO_2 functionalized TENG and MIL-125(Ti) TENG devices are found to be 6 W m^{-2} and 3.6 W m^{-2}, respectively. A significant improvement is also found in the power density of the NO_2 functionalized TENG $\sim$ 6 W m^{-2} and MIL-125(Ti) TENG $\sim$ 3.6 W m^{-2}, when compared with pristine silicone TENG devices.

The frequency dependence on the output response of the TENG was analyzed from 1 Hz to 6 Hz and is illustrated in Fig. 5f, and it is found that 4 Hz is considered the optimal frequency for the developed TENG device. The frequency response of the TENG is in good agreement with previously reported literature.[77] The key factor for using TENG devices in real-life applications is their long-term stability and durability. The voltage response of the MIL-125(Ti)-NH_2@silicone TENG was tested over 10 000 cycles using an in-house developed tapping machine at a constant frequency of 4 Hz. The TENG device responses were recorded a few seconds at every 1k, 3k, 5k and 10k cycles, and results are shown in Fig. 5g and Video S1 (ESI†). The voltage response remains consistent during the stability test, indicating the high stability of the fabricated TENG device. The variation in the TENG output stability is due to the difference in the applied force with machine and manual hand tapping.

The fabricated TENG DC output was used to charge various capacitors ranging from 3.3 μF to 100 μF capacitance values for 100 s, and its corresponding charging profile is shown in Fig. 6(a and b). The behaviour of stored charge (Q) and charged voltage (V) was estimated by using the formula $Q = CV$, where C represents the load capacitance. Hence as the load capacitance increases, the stored charge proportionally increases, and the charged voltage exhibits an inverse trend.[78]

Furthermore, the fabricated MIL-125(Ti)-NH_2@silicone TENG device was used to run low-power electronic devices commonly used in daily life. The circuit diagram used to power electronic devices, which comprises a rectifier and a capacitor, is depicted in Fig. 6c. The DC output of the developed TENG devices was used to illuminate 480 LEDs connected in series under hand tapping (Video S1, ESI†). Fig. 6d shows the ON and OFF states of the LEDs. Under continuous tapping of the fabricated TENG device, the stored charge in the capacitor of 27 μF was used to run low-power electronic devices such as hygrometers, wristwatches, and calculators, and the corresponding photographs of the ON and OFF states are as shown in Fig. 6(e–g). The corresponding videos of powering the electronic devices are given in Videos S2–S5 (ESI†).

4. MIL-125(Ti)-NH_2@silicone TENG based smart hygiene system

Public washroom hygiene is a vital aspect of public health and well-being. A clean and well-maintained public washroom can safeguard community health by minimizing the transmission of various infectious diseases, such as *E. coli*, norovirus, hepatitis, *etc.*[79–81] Therefore, a consistent cleaning schedule forms the basis for keeping the washroom in hygienic conditions. It not only safeguards public health and fosters a positive user experience, but it can also instill a sense of overall cleanliness in the individuals. Instead of relying on cleaners for constant monitoring, a reliable and efficient washroom hygiene sensing system would promote restroom maintenance. This proactive approach would free up cleaners to focus on deep cleaning and other crucial tasks, ultimately leading to a more consistently hygienic environment.

Hence, in the present work, we introduce a novel TENG-based door sensor that tracks washroom usage sustainably based on the movement (closing–opening) of the door. This real-time data alerts the cleaning committee, thus promoting a clean and healthy washroom. In this modern era, door sensors are a reliable invention that utilizes changes in motion, magnetic field, or proximity to detect whether the door is open or closed. These sensors play a crucial role in various applications such as securing our homes, triggering automatic lighting, and optimizing the energy usage of the building.

The prototype TENG-based door sensor includes a TENG device, an Arduino board, and a Blynk app. The voltage pulse signal generated by the TENG device during the door activity is fed to the Arduino board, and the signal is further transmitted to the Blynk IoT app, which triggers a notification on the smartphone. The MIL-125(Ti)-NH_2@silicone, along with the aluminum electrode, is fixed to the door, whereas the other triboelectric layer of aluminum is attached to the frame of the door, as shown in Fig. 7(a). The aluminum attached to the door serves as a ground electrode, thus enabling the TENG to work

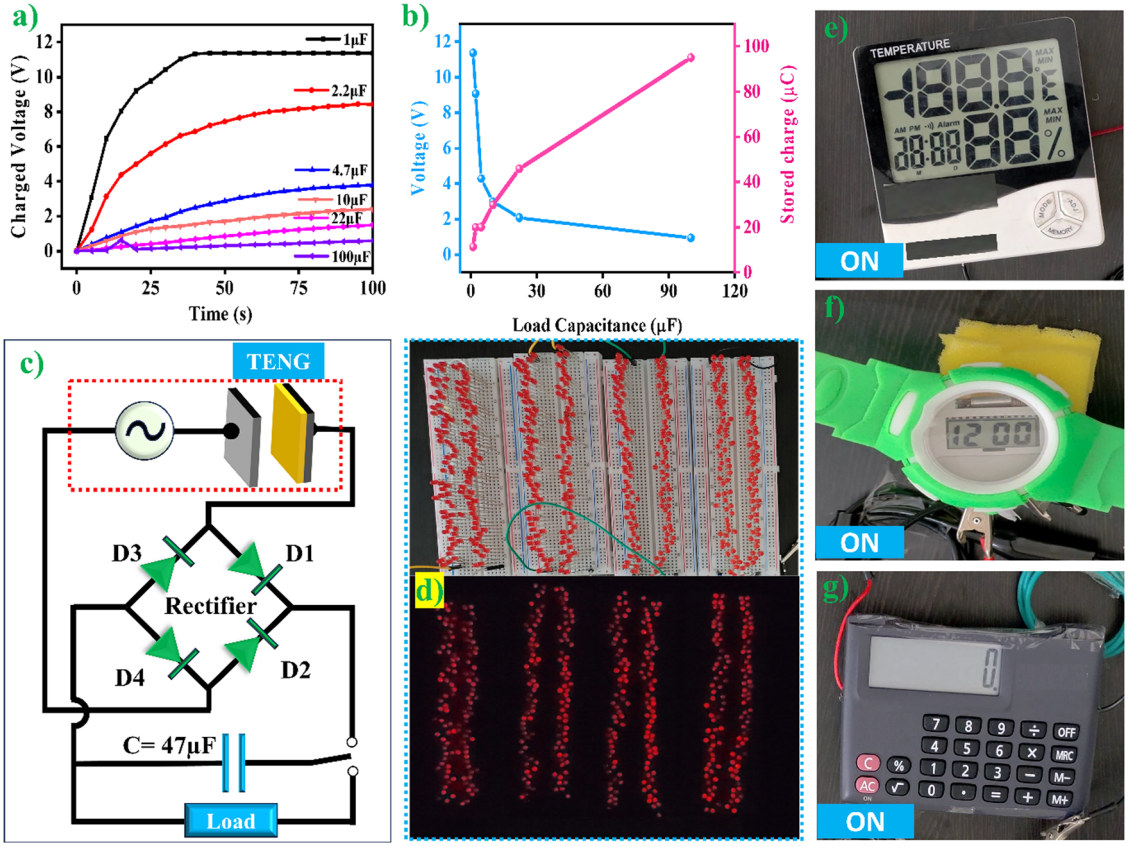

Fig. 6 (a) Charging profile of various capacitors. (b) Charged voltage and stored charge as a function of capacitance. (c) Rectifier circuit used for TENG output storage, ON states of (d) 480 LEDs connected in series, (e) a hygrometer, (f) a wristwatch, and (g) a calculator.

in single-electrode mode, as shown in Fig. 7(b). As the door closes, the triboelectric effect generates positive and negative charges on the aluminum layer and MIL-125(Ti)-NH_2@silicone. As the door opens, a potential difference is induced across the electrode due to electrostatic induction. The Arduino board connected to the TENG reads this voltage fluctuation. The Arduino board is programmed to count the number of times the door closes and opens based on the voltage fluctuation, one cycle for each close and open sequence, where it is fed to the Blynk IoT app connected *via* Wi-Fi. Upon surpassing the predetermined threshold cycles, the Blynk app automatically triggers a notification "Usage of washroom exceeded" alerting the

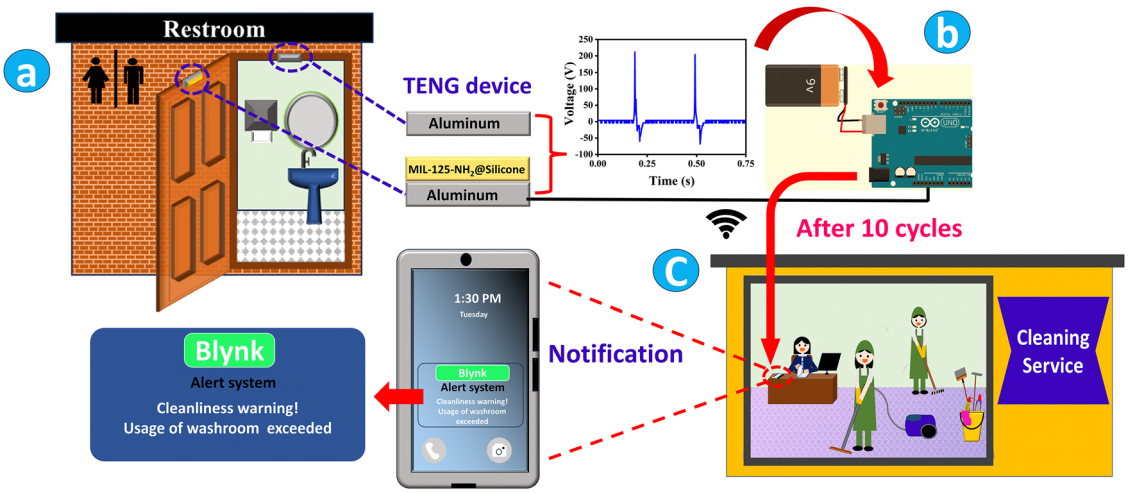

Fig. 7 (a) As prepared MIL-125(Ti)-NH_2@silicone and aluminum attached to the door and frame. (b) The device in single electrode mode and connected to an Arduino board. (c) After 10 cycles of closing and opening, a notification is received on a smartphone.

cleaning committee, as illustrated in Fig. 7(c), and the same is presented in Video S6 (ESI†). Thus, the proposed TENG-based door sensor ensures the public washrooms remain clean, hygienic, and user-friendly, ultimately eliminating all the negative connotations often associated with public washrooms.

5. Conclusions

In this work, functionalized MIL-125(Ti) materials with electron-donating (NH_2) and electron-withdrawing (NO_2) groups were incorporated into a silicone matrix to study the underlying relationship between functional groups and TENG output performance. The output performance of the TENG device follows the trend silicone < MIL-125(Ti)@silicone < MIL-125(Ti)-NO_2@silicone < MIL-125(Ti)-NH_2@silicone, which is in accordance with measurements of surface roughness, work function, and dielectric constant. The MIL-125(Ti)-NH_2@silicone produced maximum open circuit voltage and short circuit current of 512 V and 130 μA, respectively. At an external resistance of 10 MΩ, the MIL-125(Ti)-NH_2@silicone based TENG device attained a peak power density of 6.75 W m^{-2} twice the power density of the pure silicone-based TENG. The 1.5% w/w MIL-125(Ti) optimal mass ratio for TENG performance. The stability of the device over 10 000 cycles reveals that the output response remains constant. The fabricated device was used to light up 480 LEDs and run low-power electronic devices. Finally, we introduce a novel TENG-based door sensor by utilizing MIL-125(Ti)-NH_2@silicone and aluminum as a triboelectric layer, which tracks washroom usage sustainably based on the movement of the door. This real-time data alerts the cleaning committee, thus promoting a clean and healthy washroom.

Data availability

The data that support the findings of this study are available from the corresponding author upon reasonable request.

Conflicts of interest

The authors declare no conflict of interest.

Acknowledgements

The authors K. U. K. and R. R. K. would like to thank the Department of Physics and the Centre for Research and Instrument Facility (CRIF), NIT Warangal, for providing their research facilities. D. S. L. acknowledges the Basic Science Research Program through the National Research Foundation of Korea (NRF) funded by the Ministry of Education (RS-2018-NR031057). Y. K. M. acknowledges the funding from the NANOCHEM (National Infrastructure UFM 5229-00010B, NANOCHEM, Denmark), BHJ Fonden, and Fabrikant Mads Clausen Fonden, Denmark.

References

1 X. Cao, Y. Xiong, J. Sun, X. Xie, Q. Sun and Z. L. Wang, *Nano-Micro Lett.*, 2022, **15**, 1–41.
2 A. Kakim, A. Nurkesh, B. Sarsembayev, D. Dauletiya, A. Balapan, Z. Bakenov, A. Yeshmukhametov, G. Kalimuldina, A. Kakim, A. Nurkesh, B. Sarsembayev, D. Dauletiya, A. Balapan, Z. Bakenov, A. Yeshmukhametov and G. Kalimuldina, *Adv. Sens. Res.*, 2024, 2300163.
3 L. Zhou, D. Liu, J. Wang and Z. L. Wang, *Friction*, 2020, **8**, 481–506.
4 Z. Gao, Y. Zhou, J. Zhang, J. Foroughi, S. Peng, R. H. Baughman, Z. L. Wang and C. H. Wang, *Adv. Mater.*, 2024, 2404492.
5 C. Liu, R. Gu, J. Yang, L. Luo, M. Chen, Y. Xiong, Z. Huo, Y. Liu, K. Zhang, J. Gong, L. Wei, Y. Lei, Z. L. Wang and Q. Sun, *Adv. Funct. Mater.*, 2024, 2405104.
6 S. M. Sohel Rana, O. Faruk, M. Robiul Islam, T. Yasmin, K. Zaman and Z. L. Wang, *Coord. Chem. Rev.*, 2024, **507**, 215741.
7 R. K. Rajaboina, U. K. Khanapuram and A. Kulandaivel, *Adv. Sens. Res.*, 2024, **3**, 2400045.
8 S. N. Alam, A. Ghosh, P. Shrivastava, U. Shukla, K. Garg, A. C. Edara and N. Sahoo, *Nano-Struct. Nano-Objects*, 2023, **34**, 100980.
9 W. G. Kim, D. W. Kim, I. W. Tcho, J. K. Kim, M. S. Kim and Y. K. Choi, *ACS Nano*, 2021, **15**, 258–287.
10 J. Hu, M. Iwamoto and X. Chen, *Nano-Micro Lett.*, 2023, **16**, 1–25.
11 C. Cao, Z. Li, F. Shen, Q. Zhang, Y. Gong, H. Guo, Y. Peng and Z. L. Wang, *Energy Environ. Sci.*, 2024, **17**, 885–924.
12 S. A. Lone, K. C. Lim, K. Kaswan, S. Chatterjee, K. P. Fan, D. Choi, S. Lee, H. Zhang, J. Cheng and Z. H. Lin, *Nano Energy*, 2022, **99**, 107318.
13 Y. Wang, X. Jin, W. Wang, J. Niu, Z. Zhu and T. Lin, *ACS Appl. Electron. Mater.*, 2021, **3**, 532–549.
14 S. Potu, A. Kulandaivel, B. Gollapelli, U. K. Khanapuram and R. K. Rajaboina, *Mater. Sci. Eng., R*, 2024, **161**, 100866.
15 M. T. Rahman, S. M. S. Rana, M. Salauddin, M. A. Zahed, S. Lee, E. S. Yoon and J. Y. Park, *Nano Energy*, 2022, **100**, 107454.
16 S. M. S. Rana, M. A. Zahed, M. T. Rahman, M. Salauddin, S. H. Lee, C. Park, P. Maharjan, T. Bhatta, K. Shrestha and J. Y. Park, *Adv. Funct. Mater.*, 2021, **31**, 2105110.
17 A. Chen, C. Zhang, G. Zhu, Z. Lin Wang, A. Chen, C. Zhang, G. Zhu and Z. L. Wang, *Adv. Sci.*, 2020, **7**, 2000186.
18 M. Shanbedi, H. Ardebili and A. Karim, *Prog. Polym. Sci.*, 2023, **144**, 101723.
19 G. M. Rani, C. M. Wu, K. G. Motora, R. Umapathi and C. R. M. Jose, *Nano Energy*, 2023, **108**, 108211.
20 A. Babu, K. Ruthvik, P. Supraja, M. Navaneeth, K. U. Kumar, R. R. Kumar, K. Prakash and N. Raju, *J. Mater. Sci.: Mater. Electron.*, 2023, **34**, 2195.
21 R. A. Shaukat, Q. M. Saqib, J. Kim, H. Song, M. U. Khan, M. Y. Chougale, J. Bae and M. J. Choi, *Nano Energy*, 2022, **96**, 107128.

22 S. M. S. Rana, M. T. Rahman, M. A. Zahed, S. H. Lee, Y. Do Shin, S. Seonu, D. Kim, M. Salauddin, T. Bhatta, K. Sharstha and J. Y. Park, *Nano Energy*, 2022, **104**, 107931.
23 A. Babu, S. Gupta, R. Katru, N. Madathil, A. Kulandaivel, P. Kodali, H. Divi, H. Borkar, U. K. Khanapuram and R. K. Rajaboina, *Energy Technol.*, 2024, **12**, 2400796.
24 G. M. Rani, S. M. Ghoreishian, K. S. Ranjith, S. H. Park, M. Lee, R. Umapathi, Y. K. Han and Y. S. Huh, *Adv. Mater. Technol.*, 2023, **8**, 2300685.
25 A. Babu, L. Bochu, S. Potu, R. Kaja, N. Madathil, M. Velpula, A. Kulandaivel, U. K. Khanapuram, R. K. Rajaboina, H. Divi, P. Kodali, B. Ketharachapalli and R. Ammanabrolu, *ACS Sustainable Chem. Eng.*, 2023, **11**, 16806–16817.
26 V. F. Yusuf, N. I. Malek and S. K. Kailasa, *ACS Omega*, 2022, **7**, 44507–44531.
27 P. K. Nitha and A. Chandrasekhar, *Mater. Today Energy*, 2023, **37**, 101393.
28 Z. Shao, J. Chen, Q. Xie and L. Mi, *Coord. Chem. Rev.*, 2023, **486**, 215118.
29 R. K. Rajaboina, U. K. Khanapuram, V. Vivekananthan, G. Khandelwal, S. Potu, A. Babu, N. Madathil, M. Velpula and P. Kodali, *Small*, 2023, 2306209.
30 S. M. Sohel Rana, M. Abu Zahed, M. Robiul Islam, O. Faruk, H. Su Song, S. Hoon Jeong and J. Yeong Park, *Chem. Eng. J.*, 2023, **473**, 144989.
31 Y. Guo, Y. Cao, Z. Chen, R. Li, W. Gong, W. Yang, Q. Zhang and H. Wang, *Nano Energy*, 2020, **70**, 104517.
32 Y. M. Wang, X. Zhang, C. Liu, L. Wu, J. Zhang, T. Lei, Y. Wang, X. B. Yin and R. Yang, *Nano Energy*, 2023, **107**, 108149.
33 N. S. Abdul Mubarak, K. Y. Foo, R. Schneider, R. M. Abdelhameed and S. Sabar, *J. Environ. Chem. Eng.*, 2022, **10**, 106883.
34 X. Zhang, K. Yue, R. Rao, J. Chen, Q. Liu, Y. Yang, F. Bi, Y. Wang, J. Xu and N. Liu, *Appl. Catal., B*, 2022, **310**, 121300.
35 Y. Zhao, W. Cai, J. Chen, Y. Miao and Y. Bu, *Front. Chem.*, 2019, **7**, 490118.
36 V. P. Kallupadi, H. Varghese, U. N. S. Hareesh and A. Chandran, *Adv. Funct. Mater.*, 2025, **35**, 2411855.
37 G. Khandelwal, N. P. Maria Joseph Raj, V. Vivekananthan and S.-J. Kim, *iScience*, 2021, **24**, 102064.
38 T. Wang, Q. Zhu, Q. Zhu, Q. Yang, S. Wang and L. Luo, *Nanoscale Adv.*, 2022, **4**, 4314–4320.
39 J. Mo, Y. Liu, Q. Fu, C. Cai, Y. Lu, W. Wu, Z. Zhao, H. Song, S. Wang and S. Nie, *Nano Energy*, 2022, **93**, 106842.
40 Y. Zhang, T. Kang, X. Han, W. Yang, W. Gong, K. Li and Y. Guo, *Nano Energy*, 2023, **111**, 108433.
41 S. H. Sohn, G. J. Choi and I. K. Park, *Chem. Eng. J.*, 2023, **475**, 145860.
42 V. P. Kallupadi, H. Varghese, U. N. S. Hareesh and A. Chandran, *Adv. Funct. Mater.*, 2024, 2411855.
43 N. J. Castellanos, Z. Martinez Rojas, H. A. Camargo, S. Biswas and G. Granados-Oliveros, *Transition Met. Chem.*, 2019, **44**, 77–87.
44 C. H. Hendon, D. Tiana, M. Fontecave, C. Sanchez, L. D'arras, C. Sassoye, L. Rozes, C. Mellot-Draznieks and A. Walsh, *J. Am. Chem. Soc.*, 2013, **135**, 10942–10945.
45 K. Fabrizio, E. L. Gormley, A. M. Davenport, C. H. Hendon and C. K. Brozek, *Chem. Sci.*, 2023, **14**, 8946–8955.
46 M. Dan-Hardi, C. Serre, T. Frot, L. Rozes, G. Maurin, C. Sanchez and G. Férey, *J. Am. Chem. Soc.*, 2009, **131**, 10857–10859.
47 X. Zhang, K. Yue, R. Rao, J. Chen, Q. Liu, Y. Yang, F. Bi, Y. Wang, J. Xu and N. Liu, *Appl. Catal., B*, 2022, **310**, 121300.
48 Y. Fu, D. Sun, Y. Chen, R. Huang, Z. Ding, X. Fu and Z. Li, *Angew. Chem., Int. Ed.*, 2012, **51**, 3364–3367.
49 C. Zlotea, D. Phanon, M. Mazaj, D. Heurtaux, V. Guillerm, C. Serre, P. Horcajada, T. Devic, E. Magnier, F. Cuevas, G. Férey, P. L. Llewellyn and M. Latroche, *Dalton Trans.*, 2011, **40**, 4879–4881.
50 B. Han and A. Chakraborty, *Int. J. Heat Mass Transfer*, 2022, **186**, 122473.
51 J. Wang, A. S. Cherevan, C. Hannecart, S. Naghdi, S. P. Nandan, T. Gupta and D. Eder, *Appl. Catal., B*, 2021, **283**, 119626.
52 J. Zhu, P. Z. Li, W. Guo, Y. Zhao and R. Zou, *Coord. Chem. Rev.*, 2018, **359**, 80–101.
53 X. Han, X. Yang, G. Liu, Z. Li and L. Shao, *Chem. Eng. Res. Des.*, 2019, **143**, 90–99.
54 M. Sohail, Y.-N. Yun, E. Lee, S. K. Kim, K. Cho, J.-N. Kim, T. W. Kim, J.-H. Moon and H. Kim, *Cryst. Growth Des.*, 2017, **17**, 1208–1213.
55 M. A. Nasalevich, R. Becker, E. V. Ramos-Fernandez, S. Castellanos, S. L. Veber, M. V. Fedin, F. Kapteijn, J. N. H. Reek, J. I. van der Vlugt and J. Gascon, *Energy Environ. Sci.*, 2015, **8**, 364–375.
56 Z. Liu, C. Wang, Y. Wu, L. Geng, X. Zhang, D. Zhang, H. Hu, Y. Zhang, X. Li, W. Liu and P. Na, *Polyhedron*, 2021, **196**, 114980.
57 S. Hu, M. Liu, K. Li, Y. Zuo, A. Zhang, C. Song, G. Zhang and X. Guo, *CrystEngComm*, 2014, **16**, 9645–9650.
58 H. T. Flakus, *J. Mol. Struct.*, 1981, **72**, 107–117.
59 Z. Wu, X. Huang, H. Zheng, P. Wang, G. Hai, W. Dong and G. Wang, *Appl. Catal., B*, 2018, **224**, 479–487.
60 Y. Zhao, W. Cai, J. Chen, Y. Miao and Y. Bu, *Front. Chem.*, 2019, **7**, 1–10.
61 Y. He, T. Lv, B. Xiao, B. Liu, T. Zhou, J. Zhang, Y. Zhang, G. Zhang and Q. Liu, *J. Mater. Chem. C*, 2023, **11**, 6800–6818.
62 B. Ni, X. Cai, J. Lin, Y. Li, S. Huang, Z. Li and Y. Zhang, *J. Phys. Chem. C*, 2019, **123**, 653–664.
63 S.-N. Kim, J. Kim, H.-Y. Kim, H.-Y. Cho and W.-S. Ahn, *Catal. Today*, 2013, **204**, 85–93.
64 X. Zhang, K. Yue, R. Rao, J. Chen, Q. Liu, Y. Yang, F. Bi, Y. Wang, J. Xu and N. Liu, *Appl. Catal., B*, 2022, **310**, 121300.
65 S.-N. Kim, J. Kim, H.-Y. Kim, H.-Y. Cho and W.-S. Ahn, *Catal. Today*, 2013, **204**, 85–93.
66 V. L. Vilesh and S. Ganesanpotti, *J. Electron. Mater.*, 2022, **51**, 3237–3247.
67 N. Madathil, S. Potu, J. Pani, L. Bochu, A. Babu, H. Borkar, P. Kodali, U. K. Khanapuram and R. K. Rajaboina, *ACS Appl. Electron. Mater.*, 2024, **6**, 5574.

68 B.-I. Ciubotaru, M.-F. Zaltariov, M. Dascalu, A. Bele, A. Bargan and M. Cazacu, *React. Funct. Polym.*, 2024, **194**, 105792.
69 S. Kaur and D. P. Singh, *J. Alloys Compd.*, 2022, **918**, 165500.
70 J. Ye and J. C. Tan, *Nano Energy*, 2023, **114**, 108687.
71 Q. Xi, Z. Chen, Y. Li, F. Liu and Y. Guo, *ACS Appl. Electron. Mater.*, 2023, **5**, 5215–5223.
72 H. Kim, S. M. S. Rana, M. Robiul Islam, O. Faruk, K. Shrestha, G. B. Pradhan and J. Y. Park, *Chem. Eng. J.*, 2024, **491**, 151980.
73 S. M. S. Rana, M. T. Rahman, M. A. Zahed, S. H. Lee, Y. Do Shin, S. Seonu, D. Kim, M. Salauddin, T. Bhatta, K. Sharstha and J. Y. Park, *Nano Energy*, 2022, **104**, 107931.
74 S. Sarfudeen, P. K. Nitha, S. A. Basith, M. Varghese, P. Jhariat, A. Chandrasekhar and T. Panda, *ACS Appl. Mater. Interfaces*, 2024, **16**, 24851–24862.
75 M. T. Rahman, S. S. Rana, M. A. Zahed, S. Lee, E. S. Yoon and J. Y. Park, *Nano Energy*, 2022, **94**, 106921.
76 Z. Chen, Y. Cao, W. Yang, L. An, H. Fan and Y. Guo, *J. Mater. Chem. A*, 2022, **10**, 799–807.
77 M. Navaneeth, S. Potu, A. Babu, B. Lakshakoti, R. K. Rajaboina, U. Kumar K, H. Divi, P. Kodali and K. Balaji, *ACS Sustainable Chem. Eng.*, 2023, **11**, 12145–12154.
78 Y. Yao, T. Jiang, L. Zhang, X. Chen, Z. Gao and Z. L. Wang, *ACS Appl. Mater. Interfaces*, 2016, **8**, 21398–21406.
79 S. E. Abney, K. R. Bright, J. McKinney, M. K. Ijaz and C. P. Gerba, *J. Appl. Microbiol.*, 2021, **131**, 2705–2714.
80 S. W. B. Newsom, *The Lancet*, 1972, **300**, 700–703.
81 R. G. Sinclair, C. Y. Choi, M. R. Riley and C. P. Gerba, *Advances in Applied Microbiology*, Academic Press, 2008, vol. 65, pp. 249–269.